Cement and Concrete Research 42 (2012) 855–864

Contents lists available at SciVerse ScienceDirect

Cement and Concrete Research

journal homepage: http://ees.elsevier.com/CEMCON/default.asp

X-ray microtomography shows pore structure and tortuosity in alkali-activated binders

John L. Provis [a,*], Rupert J. Myers [a], Claire E. White [a], Volker Rose [b], Jannie S.J. van Deventer [a,c]

[a] Department of Chemical & Biomolecular Engineering, University of Melbourne, Victoria 3010, Australia
[b] Advanced Photon Source, Argonne National Laboratory, 9700 South Cass Ave, Argonne IL 60439, USA
[c] Zeobond Pty Ltd, P.O. Box 210, Somerton, Victoria 3062, Australia

ARTICLE INFO

Article history:
Received 22 February 2011
Accepted 13 March 2012

Keywords:
Alkali activated cement (D)
Microstructure (B)
X-ray microtomography
Transport properties (C)

ABSTRACT

Durability of alkali-activated binders is of vital importance in their commercial application, and depends strongly on microstructure and pore network characteristics. X-ray microtomography (μCT) offers, for the first time, direct insight into microstructural and pore structure characteristics in three dimensions. Here, μCT is performed on a set of sodium metasilicate-activated fly ash/slag blends, using a synchrotron beamline instrument. Segmentation of the samples into pore and solid regions is then conducted, and pore tortuosity is calculated by a random walker method. Segmented porosity and diffusion tortuosity are correlated, and vary as a function of slag content (slag addition reduces porosity and increases tortuosity), and sample age (extended curing gives lower porosity and higher tortuosity). This is particularly notable for samples with ≥50% slag content, where a space-filling calcium (alumino)silicate hydrate gel provides porosity reductions which are not observed for the sodium aluminosilicate ('geopolymer') gels which do not chemically bind water of hydration.

1. Introduction

The class of binders known as alkali-activated materials, including 'geopolymers', provides an environmentally friendly alternative to conventional cements such as ordinary Portland cement (OPC) [1,2]. In particular, alkali activation technology offers reduced CO_2 emissions (by up to 80% relative to OPC), and is primarily based around the use of industrial wastes or clays, including fly ash (FA), granulated ground blast furnace slag (GGBFS) and metakaolin, as precursors [3,4]. However, depending on the composition, fineness, mineralogy and particle morphology of the precursor materials selected, the properties of the binder can change significantly [5,6]. Alkali-activated cements with high slag content predominantly form a calcium silicate hydrate (C-S-H) gel with Al and alkali substitution, whereas those that are primarily based on fly ash or metakaolin form an amorphous aluminosilicate polymeric ('geopolymer') matrix [7,8]. Blended ash/slag binders are attracting attention at present due to the favourable combinations of properties which can be obtained through the coexistence of the two gel types [8–12], but the exact nature of the gel coexistence regimes and phenomena are not yet well understood.

Durability is critical to the commercial application and viability of any construction material, and is closely related to cement and concrete microstructure. Tortuous microstructures with narrow, isolated pores inhibit the diffusion of aggressive substances, in particular acids, carbonate or chloride, through concrete. Understanding the microstructural characteristics of the binder is therefore vitally important in enabling the commercial-scale uptake of alkali-activation technology [8]. Key microstructural properties of a binder include the porosity, tortuosity and extent of percolation of the pore network [13,14], but neither of these last two parameters have previously been able to be experimentally determined for an alkali-activated binder.

Alkali-activated binders are often highly heterogeneous due to the variable chemical and physical nature of the particles present in the fly ash used as a precursor [6], and the complex reaction process taking place during alkali activation [15]. The hardened binders are believed to contain pores of characteristic diameters ranging from below 10 nm up to approximately 10 μm [13,16,17], which can lead to significant complexities in the pore geometry. The pore networks in alkali-activated cements and OPC have previously been probed by conventional techniques such as mercury (or Wood's metal) intrusion porosimetry, gas sorption and microscopy, as well as indirectly by accelerated permeability or penetration testing. However, the major shortcoming of these conventional techniques is that they cannot provide the three-dimensional information which is required to accurately determine tortuosity and connectivity.

X-ray microtomography (μCT) is a technique which has provided valuable information in the analysis of pore networks in Portland cement [14,18–24], among many other areas of materials and biomaterials research as reviewed in [25], but which has not previously been applied

---

[*] Corresponding author. Tel.: +61 3 8344 8755; fax: +61 3 8344 4153.
E-mail address: jprovis@unimelb.edu.au (J.L. Provis).

0008-8846/$ – see front matter © 2012 Elsevier Ltd. All rights reserved.
doi:10.1016/j.cemconres.2012.03.004

to the analysis of the structure of alkali-activated binders. In particular, this technique can provide geometrically meaningful measurements of the tortuosity of hardened cements [14,24].

As with most analytical techniques, μCT has some significant limitations despite its advantages. Perhaps its greatest disadvantage is the trade-off between resolution and specimen size. Due to a combination of issues related to X-ray absorption contrast, data handling and sample manipulation [25], ultra-high-resolution X-ray tomography ("nanotomography") data for alkali-activated binders have only been obtained for very small samples (up to a diameter of several microns) at present, using specialised synchrotron radiation-based instrumentation [26]. Alternative approaches such as phase contrast tomography and focused ion beam tomography are also beginning to find application in the analysis of cement binder nanostructures, each providing advantages and disadvantages when compared with absorption-contrast tomography [19,27]. Traditional microtomography has been conducted using millimetre-sized Portland cement samples with a voxel resolution as fine as 0.5 μm [14], and a resolution of 0.75 μm is used here. This means that the identification and characterisation of a large fraction of the pore network in alkali-activated binders, which consists of nanometre-sized pores [13,26], are not possible using this technique. However, larger capillary pores are believed to dominate mass-transfer behaviour in geopolymer binders [13], and these pores are more readily observable in μCT.

The aim of this study is therefore to characterise the pore structures of alkali-activated binders using synchrotron radiation X-ray microtomography, to understand the evolution of the microstructure and pore network during the first 45 days of curing. Samples are synthesised across a range of GGBFS/FA ratios, providing for the first time information regarding the roles of the two different types of gel (calcium-dominated and aluminosilicate-dominated), and the effect of curing time, in determining the porosity and pore tortuosity of alkali-activated binders.

2. Materials and methods

2.1. Sample synthesis and experimental details

The samples used in this study were generated by alkali silicate activation of fly ash (FA; Gladstone Power Station, Australia) and ground granulated blast furnace slag (GGBFS; Independent Cement & Lime, Australia), with compositions as shown in Table 1. Precursor blends used were 100% GGBFS; 75% GGBFS/25% FA; 50% GGBFS/50% FA; 25% GGBFS/75% FA; and 100% FA. Each sample was activated using solid anhydrous sodium metasilicate and tap water, at an activator concentration of 7 wt.% (i.e. 7 g Na_2SiO_3 per 100 g of FA + GGBFS) and a water to binder ratio (w/b) of 0.40. The activating solution was mixed by hand with the pre-blended solid precursors to create a uniform paste, which was transferred to polymeric tubes, sealed, and cured at 23 °C for specified times up to 45 days. To stop the reaction of samples after the desired curing times, the small monolithic samples were immersed in acetone; the sections of the samples used for analysis were taken from the regions close to the external surfaces of the monoliths, ensuring that the curing durations given this paper are as accurate as possible, as the reactions in these regions of the samples will have been halted the most effectively by the immersion in acetone. One specimen per mix was studied for each curing duration, and one volume of interest (VOI) per specimen was selected for detailed segmentation as described below.

Table 1
Compositions of fly ash and ground granulated blast furnace slag used in this investigation, from X-ray fluorescence analysis. LOI is loss on ignition at 1000 °C.

Oxide (wt.%)	FA	GGBFS
Na_2O	0.33	0.15
MgO	1.41	6.13
Al_2O_3	30.28	14.11
SiO_2	47.68	34.17
P_2O_5	0.93	0.01
SO_3	0.14	0.61
K_2O	0.47	0.32
CaO	1.84	42.10
TiO_2	1.67	0.53
Mn_3O_4	0.15	0.29
Fe_2O_3	11.26	0.34
LOI	3.7	1.2

Samples of around 1 mm in size were analysed using beamline 2-BM at the Advanced Photon Source, Argonne National Laboratory [28]. Measurements were carried out using hard X-ray synchrotron radiation (22.5 keV) in a parallel-beam configuration, with 0.12° rotation per step (1501 steps in a 180° rotation) and 0.4 s exposure time per step. Samples were mounted in small polymeric cones to enable alignment; sample size and shape were somewhat irregular, as the samples were obtained by fracturing larger monoliths, but all samples fitted within the field of view in the horizontal plane of the detector. X-ray detection was achieved with a scintillator and CCD camera, capturing 2048×2048 pixels. Tomographic data were reconstructed using an in-house developed reconstruction algorithm, including re-centring following visual inspection to ensure optimal reconstructions, using a voxel size of 0.75 μm (corresponding to the detector resolution).

2.2. Volume of interest selection and segmentation

The VOI of a tomographic reconstruction, which is the portion of the full data set chosen for segmentation (and which is, in this investigation, significantly less than the full sample size to enable data processing without severe problems due to memory limitations during computation) should be selected to be large enough to eliminate the introduction of errors due to finite size. It has previously been suggested that the minimum VOI should be at least 100 μm^3, or greater than 3 to 5 times the size of the largest distinct feature of the sample for hardened OPC pastes, to eliminate finite size error [29,30]. While these suggestions are reasonable for GGBFS-based binders, which form a C-S-H phase similar to that found in hydrated OPC, materials primarily comprised of alkali-activated fly ash display significantly different microstructures, including large unreacted fly ash particles. No μCT data sets have previously been made available for systematic series of geopolymer samples, meaning that some basic work in this area is also needed. A method that is expected to identify representative sizes for these materials involves selecting a volume that corresponds to the point where the error associated with the segmented porosity, or any other known geometrical characteristic of the sample, approaches a minimum value. The investigation of Gallucci et al. [31] uses this technique to study the characteristics of OPC cement.

The finite voxel size can introduce errors associated with identification of the porous network of the material, which is typically obtained by segmentation techniques. The distinction between pore space and silicate gel (the calcium silicate or alkali aluminosilicate binder phase) is much more difficult to determine for larger voxel sizes. This is a significant limitation of the μCT technique at present [29].

Segmentation involves selecting a threshold value to distinguish the pore space from the binder (solid) phase — and in this work, a simple global thresholding method was applied, with a single threshold value selected per data set. There is still a good deal of 'art' required in the segmentation process [25], and although there are user-independent segmentation algorithms available, their accurate application to complex materials remains an area of ongoing research. The identification and use of a 'transition point' in the greyscale histogram of all voxels in the sample is one method often used in segmentation, which involves selecting the threshold when the cumulative voxel count vs. intensity distribution for any given sample begins to rapidly increase [32]. However, this method is considerably limited for the case of a geopolymer sample, as it is unable to deal with samples that exhibit a gently sloping cumulative distribution, due to the presence of pores below the available voxel resolution, a wide range of greyscale intensities due to the presence of a variety of different unreacted fly ash particles, and/or a low extent of reaction.

Another method used in segmentation is to select the threshold using known characteristics of the pore structure. As an example, the reaction of fly ash particles will occur at the particle surface, and many fly ash particles also contain internal voids. The pore space can be more easily distinguished in these regions because the geometry can be inferred from known structures, which can enhance the accuracy of the chosen threshold. Ongoing dissolution of the surface of a fly ash particle after the geopolymer binder has hardened is known to create a distinctive pore space with a characteristic size of up to a few μm [33]. However, this method does depend on the application of discretion to identify features and select an appropriate threshold, meaning that it is less reproducible between operators and laboratories.

In this investigation, segmentation was carried out using purpose-designed routines operating in the MeVisLab 2.0 software environment. First, an appropriately sized VOI was chosen to eliminate finite size error [29]; typically 300–400 voxels^3, although smaller VOIs (minimum size used was 251 voxels^3) were used in two cases (75% fly ash/25% slag at 1 day; 100% slag at 14 days) where sample geometry or cracking was restrictive. The porosity and tortuosity data obtained from these smaller VOIs did not deviate noticeably from the expected trends, meaning that any additional errors due to the smaller VOI sizes are minimal. A comparison of the VOI size to the full tomographic reconstruction is shown in Fig. 1.

Segmentation of the VOI was performed using a combination of the transition point method and consideration of localised pore structures [25]. Identification of the transition point directly from the greyscale histogram was found to be more challenging in binders with high fly ash content, in part because the variability in brightness between the different fly ash particles meant that some showed a brightness higher, and others lower, than the dense regions of the newly-formed geopolymer gel. Selection of the threshold for segmentation based on consideration of the local pore geometry was therefore required, as illustrated in Fig. 2, where the circled fly ash particle (a cenosphere) in Fig. 2a is seen to be surrounded in part (on the right-hand side of the unreacted particle) by a porous region, which is then designated as being pore space for the purposes of determining the appropriate segmentation threshold. Identifying and analysing several regions such as this within each sample then enable the selection of the most appropriate threshold value.

However, for the 100% slag and 100% fly ash samples with 7 days of curing, consideration of the localised pore structure did not conclusively identify the appropriate threshold value. This suggests that the local 'pore' networks (as identified with the 750 nm voxel size used here) did not uniformly consist of pore space, but rather contained significant amounts of both pore and solid regions. The data for these samples are thus likely to be more limited by voxel resolution, which has in turn influenced their measured segmented porosities. The uncertainty associated with the segmented porosities chosen for these samples is significant; changing the intensity threshold for the 7-day 100% GBFS sample from 125 to 127 (on an 8-bit scale from 0 to 255) resulted in a 7% increase in the segmented porosity and a 12% decrease in the diffusion tortuosity. The thresholds used here were selected on the basis of providing the most visually realistic depiction in agreement with the current understanding of the microstructure of alkali-activated binders, but it is acknowledged that there is certainly scope for future developments in the implementation of more accurate and more advanced thresholding procedures, making use of microstructural features rather than simply using a binary division of greyscale intensity, for application to materials such as these. The use of methods such as edge-detection to identify and classify

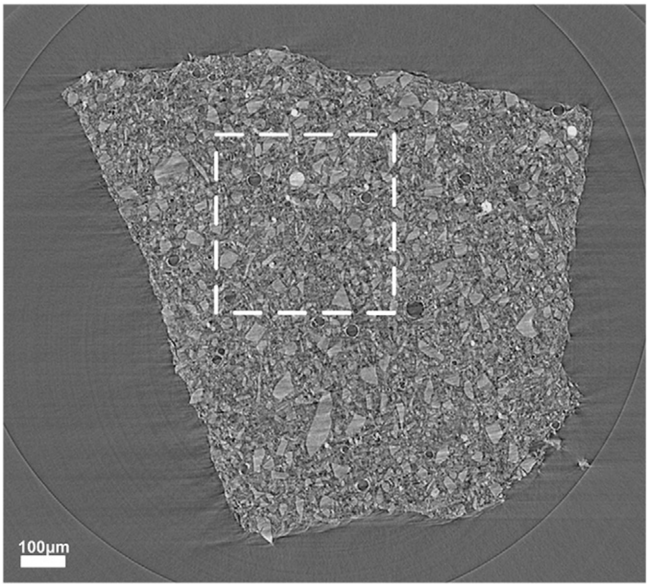

Fig. 1. A slice through the full tomographic reconstruction of the 45-day 75% GGBFS/25% FA sample, showing the relative size of the VOI selected.

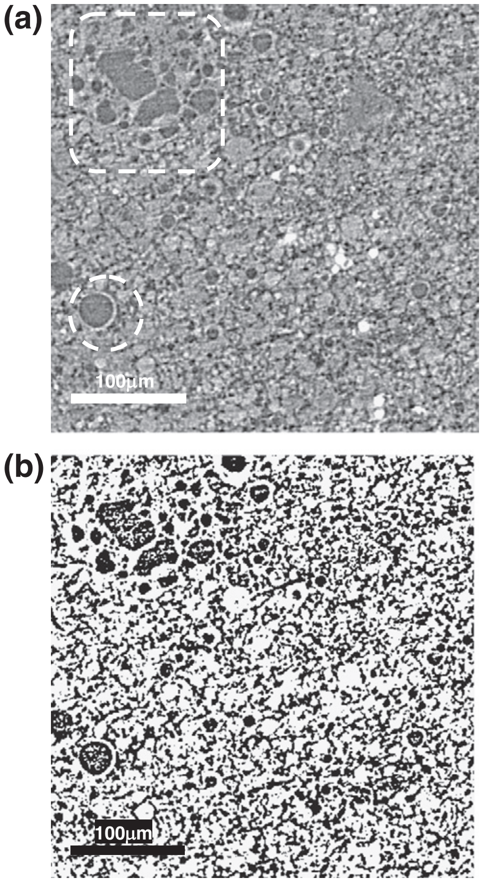

Fig. 2. Selection of the threshold by making use of a localised pore network, exemplified here for the 7-day 100% fly ash sample by the porous region surrounding the circled fly ash particle: (a) original greyscale image, (b) binary segmented image. The particle marked by the rounded rectangle is a large, complex, unreacted fly ash particle, as discussed in the text.

unreacted materials is challenging for materials with such low absorption contrast in this X-ray energy range, but does provide some interesting possibilities for future advances in data analysis in this field.

An additional complicating factor in the segmentation process for fly ash-containing samples is the correct identification of internal porosity within fly ash particles, as shown in Fig. 2a for the particle marked with a rounded rectangle (top left-hand corner of the image). This is a large particle containing multiple hollow regions, and whose outline is not clearly distinct from the surrounding binder regions — possibly due to its lower reactivity compared to the particle marked by the circle, which has continued to react after the binder has hardened, leaving an identifiable porous region immediately surrounding the spherical fly ash particle. Some regions within the particle, which are visibly identifiable as pores, appear as patchy, partially 'solid' phase regions in the segmented data set. The low X-ray absorption contrast of the low-elemental number aluminosilicate phases compared to empty space is probably responsible for this difficulty in the analysis of the larger void spaces. The presence of such particles in fly ash-containing samples may also have been a complicating factor in the determination of the correct threshold value and in analysis of the total porosity of the materials, although trial calculations with VOIs either specifically including or excluding such particles did not show significant differences in transport properties.

2.3. Pore connectivity

Three-dimensional pore connectivity data are obtained through cluster labelling, applying a modified version of the Mathematica code of Nakashima and Kayima [34] to a contiguous set of 2D image slices generated by the segmentation algorithm to represent the VOI. The connectivity determination algorithm used here is based on the work of Hoshen and Kopelman [35], and scans through each voxel in the contiguous image set in a sequential fashion, over the entire three-dimensional sample. For each pore voxel, the algorithm checks the face-adjacent voxels that have already been scanned. If the voxel is face-adjacent to another pore voxel it is labelled with a numerical identifier that is the same as that assigned to the face-adjacent voxel. If not, the pore voxel is labelled with a new numerical identifier. Only face-adjacent voxels are considered for pore connectivity; voxels which share an edge or a corner are not considered to be connected. The scan is then repeated to correct any labelling errors due to complex pore geometries. This typically requires approximately 4 h for a VOI size of 400^3 voxels using a dual-core desktop PC.

2.4. Tortuosity calculation

The segmented VOIs were then subjected to random-walker simulation to determine the physical properties of the pore network. Fig. 3 shows an example of the process undertaken, where an example of a reconstructed VOI is shown in Fig. 3a in greyscale, segmented into solid and pore regions in Fig. 3b, and the path of a random walker through the pore network in Fig. 3c. A minimum of 6000 walkers were used for each sample, with each walker moving for 400,000 timesteps, which has been determined to be well above the limit where restricted diffusion begins [36]. The displacements of the walkers were plotted as a function of the number of timesteps (τ), and the diffusion tortuosity was calculated from the inverse of the slope of this curve in the region $\tau > 50{,}000$ to eliminate data points corresponding to the unrestricted diffusion regime. The random walker simulation was implemented in Mathematica 7.0 utilising a modified version of the freely available *Rwalk.nb* script of Nakashima and Kayima [34], and a typical computation required around 10 h per sample.

To perform the simulation, a random pore voxel is chosen as the initial position of each walker. This inherently confines the walker

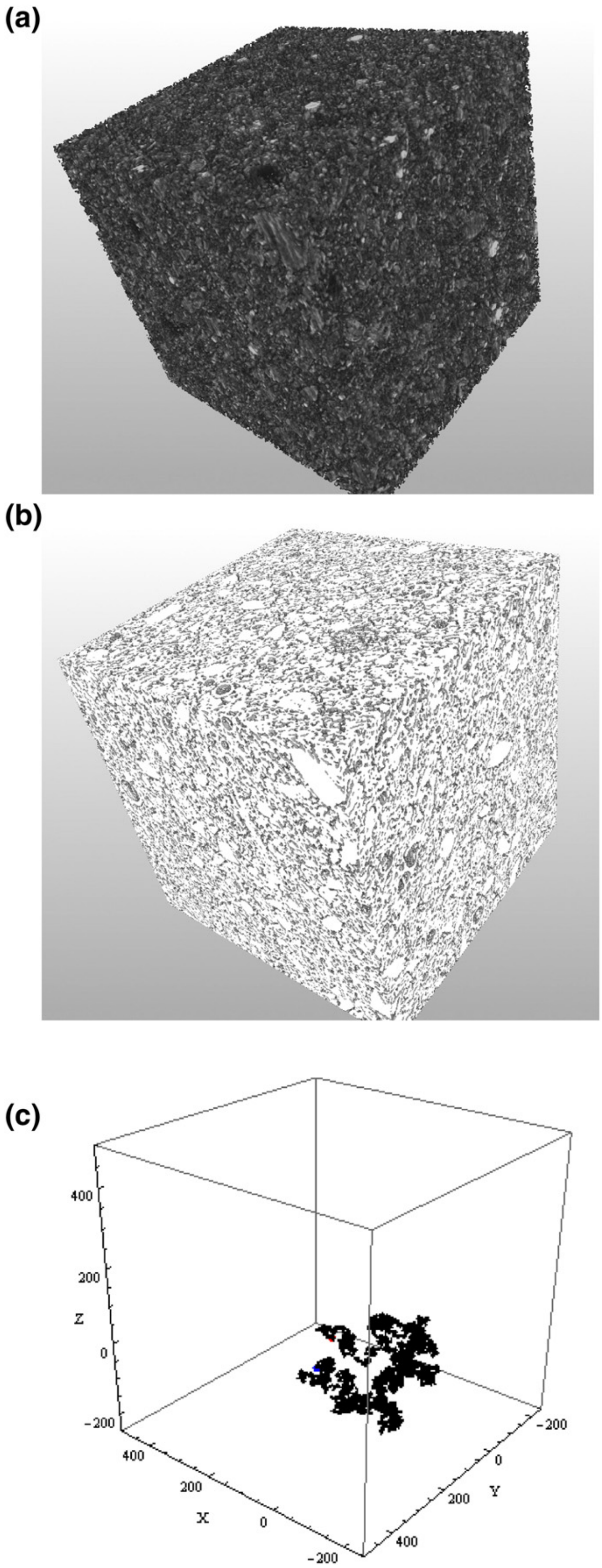

Fig. 3. Images of a cubic region of a sample (50% GGBFS/50% FA, 3 days), (a) in greyscale and (b) segmented, and (c) illustration of the path taken by one random walker through the tortuous pore network obtained by segmentation.

in the associated connected pore network as it can only migrate across voxels that have been identified as pore space. The diffusion tortuosity τ_D is measured as the ratio of the self-diffusion of a walker in free space to the self-diffusion of a walker in the porous medium, as defined in Eq. (1) [34].

$$\tau_D = \frac{D_o}{D(t)} = \frac{a^2}{\frac{d\left(r(\tau)^2\right)}{d\tau}}\, as\, t \rightarrow \infty \cup \tau \rightarrow \infty \tag{1}$$

In Eq.(1), D_o is the self-diffusivity of a random walker in free space, $D(t)$ is the self-diffusivity of a walker in the porous medium, $r(\tau)^2$ is the mean-squared displacement as a function of the number of timesteps, and a is the length parameter. Setting $a = 1$ gives the dimensionless diffusion tortuosity for a unit length of the sample [34]. By the use of Eq. (1), the restricted diffusion characteristics of these materials can be described in a geometrically meaningful manner. Restricted diffusion describes the self-diffusion of walkers for long time scales; on such time scales, the mean-squared displacement of the walker increases linearly with the number of timesteps, as it samples the full geometry of the pore network [34], leading to a constant calculated tortuosity. Tests were run for values of τ up to 10^6, and as many as 20,000 random walkers per sample; no significant changes in the tortuosity parameters obtained were observed above

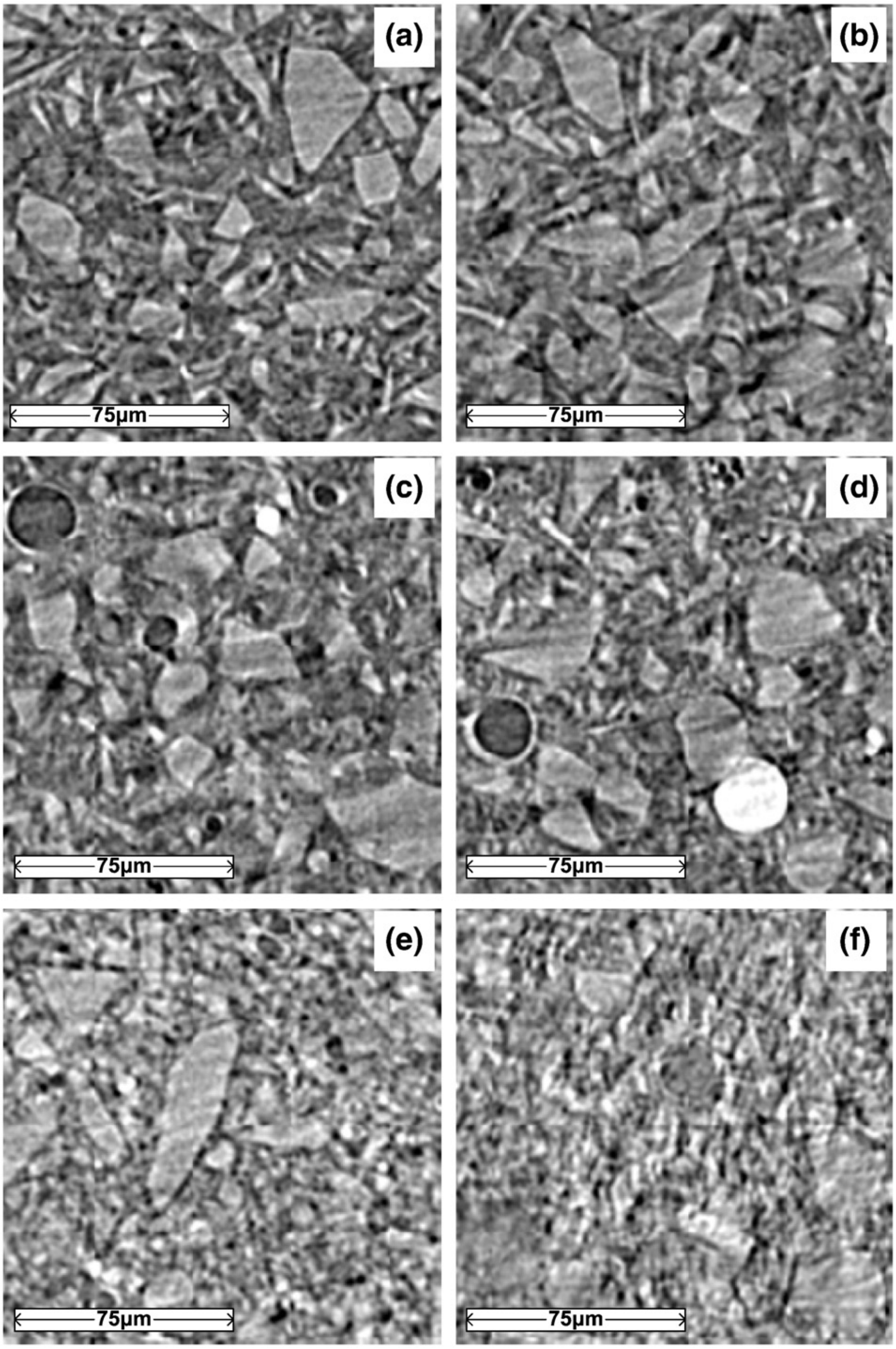

Fig. 4. Alkali-activated binder microstructures as a function of age and compositions; each image is a single slice from the reconstructed volume obtained using X-ray microtomography: (a) 100% GGBFS, 3 days; (b) 100% GGBFS, 45 days; (c) 75% GGBFS/25% FA, 3 days; (d) 75% GGBFS/25% FA, 45 days; (e) 50% GGBFS/50% FA, 3 days; (f) 50% GGBFS/50% FA, 45 days; (g) 25% GGBFS/75% FA, 3 days; (h) 25% GGBFS/75% FA, 45 days; (i) 100% FA, 3 days; (j) 100% FA, 45 days.

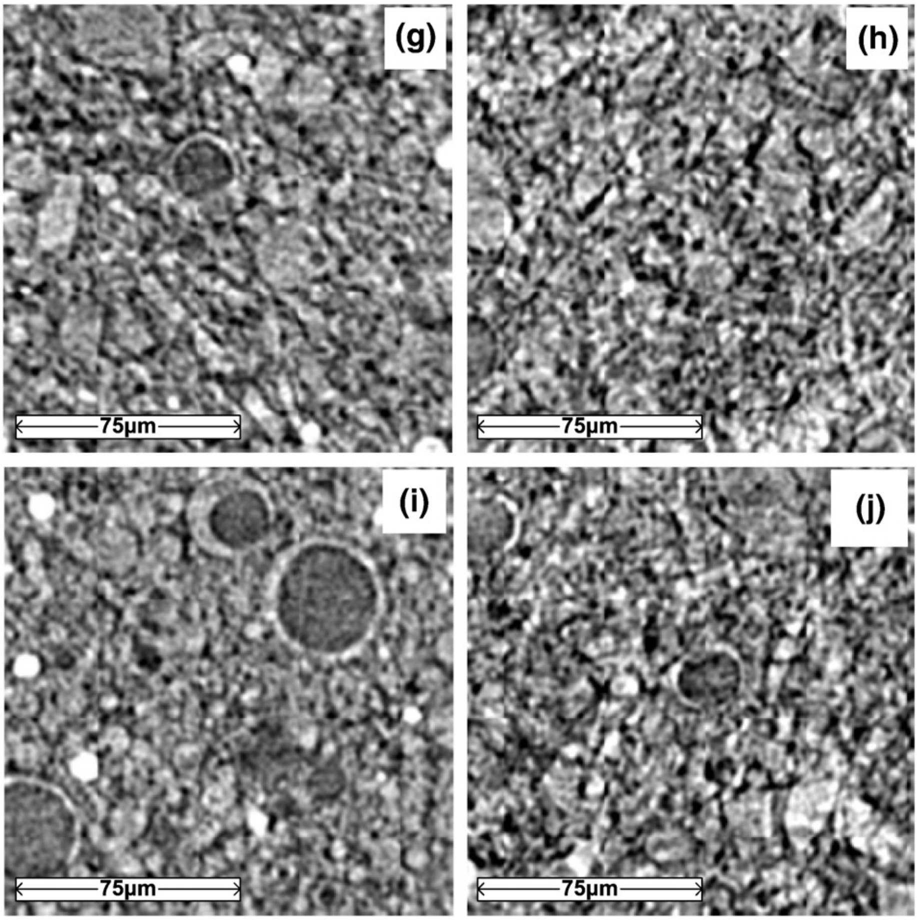

Fig. 4 (*continued*).

$\tau = 100{,}000$ or using more than 2000 walkers, so the data presented were obtained at values significantly above this cutoff to minimise uncertainty.

Fig. 3c displays the path of a single random walker through the three-dimensional pore network of one of the samples analysed. It is evident from this image that the pore geometry is complex, and that the 'ink-bottle' effect is likely to be highly significant in any traditional porosimetric analysis of this material [13], with narrow pore throats connecting larger, open volumes. The pores are also visibly irregular in shape, casting doubt on the value of applying simple geometric modifications to standard expressions as a means of describing pore networks in alkali-activated binders.

3. Results and discussion

Some of the microstructural information obtained by synchrotron radiation µCT analysis is shown in Fig. 4, which presents one slice taken from the VOI for each sample analysed at two different ages: blends of fly ash and slag in varying ratios from 100% slag to 100% fly ash, at 3 and 45 days of age. The unreacted GGBFS and fly ash particles are readily distinguished by their geometry; fly ash is comprised of polydisperse spherical particles, whereas GGBFS is visible as irregular jagged particles [6]. Also, fly ash particles can typically contain a large interior pore surrounded by a crust of ash, or can be comprised of solid spheres, some Fe-rich (and therefore brighter in the X-ray images presented), and others predominantly aluminosilicate and thus presenting lower X-ray contrast [33]. The internal voids within the hollow (including cenosphere and plerosphere) fly ash particles can be up to several tens of microns in size. The unreacted particles maintain their characteristic geometry when activated, but the reaction products generally show a lower brightness (i.e. lower X-ray absorption) due to the presence of bound water in the Ca-rich gel phases, and the presence of fine pores throughout the Ca-rich and aluminosilicate-rich gels [37]. In general, for both fly ash and GGBFS particles, the reaction occurs predominantly at the particle surface, consuming the precursor material and forming a porous partially-reacted layer [33]. For GGBFS, this layer has a lower level of Ca but is enriched in Mg, and fly ash particles tend to be surrounded either by an entirely porous region, or residual mullite crystallites, if the particle has continued to react after the binder has hardened [37]. The gel formed in both cases contains nanometre-sized pores, and appears homogeneous at the moderate resolution available here.

The microstructures shown in Fig. 4 are typical of the reconstructed sample volumes for each composition. As fly ash content increases, so does the visible fraction of spherical fly ash particles in the reconstructed sample, as expected, with a corresponding reduction in the amount of irregular GGBFS particles. The formation of large pore spaces intermixed with dense reaction products, as seen via the dark regions surrounding the unreacted precursor particles, is visible in all samples.

It is noted that the reconstructed microstructures shown in Fig. 4 do appear to contain some degree of streaking (dark bands across unreacted particles) as an artefact from the reconstruction procedure. These streaks may slightly impact the calculated tortuosity of the pore networks of the binders, because they result in the apparent presence of 'straight pores' in regions that are in fact solid, thus reducing the tortuosity. While this is certainly undesirable in terms of the analysis of the data sets, it is noted that a high tortuosity is favourable in terms of reducing the permeability of the material, and so if the tortuosities calculated here are in error due to this phenomenon, they will fall on the conservative (low) side of the actual values with regard to durability predictions. It appears that the streaking phenomenon has minimal impact on the thresholded gel microstructure, as it is most prominent in regions of very low greyscale gradient (i.e., large homogeneous particles), and the gel regions do not show visible formation of long straight pores due to this effect.

Greyscale value histograms corresponding to the VOIs in each of the panels in Fig. 4 are shown in Fig. 5. It is notable that there is effectively no separation of peaks in the histograms for any of the samples studied; this is different from the situation observed in the literature for Portland cement [31], where distinct peaks due to the different phases present are observable. The samples containing higher concentrations of fly ash show the presence of more voxels at an intensity of 256 (i.e. white voxels), which is attributed to iron-rich phases in the ash.

Although it is not straightforward to distinguish unreacted slag from newly-formed binder by a simple thresholding procedure due to the overlap in greyscale values, the visual selection of a threshold which appears to give correct classification of unreacted slag particles gives an approximate volume fraction of 35% anhydrous slag in the sample at 3 days, and only slightly lower (34%) at 45 days. Assuming a slag density of 2900 kg/m^3, this gives an approximate extent of reaction of 23% at 3 days, and very slightly more than this at 45 days. This is consistent with literature data for systems with w/b 0.45 and a metasilicate activator as measured by chemical attack [38], which showed a sharp deceleration in hydration after the first day, with 23% hydration after 3 days and 25% after 7 days. Extent of reaction data are much more difficult to extract from the fly ash-containing samples due to the lack of contrast between unreacted particles and the newly formed binder regions; more sophisticated particle-detection algorithms need to be adapted to this task, which is by no means a trivial one, and is not attempted here.

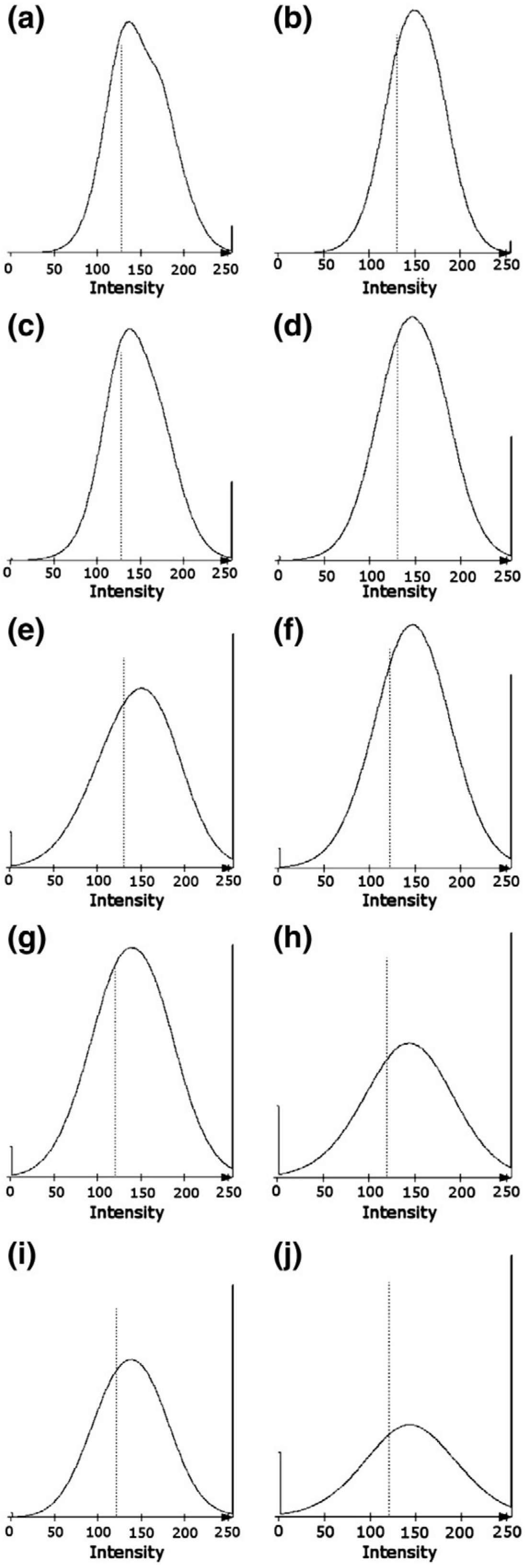

Fig. 5. Greyscale histograms for the VOIs in each sample; labels (a)–(j) correspond to the same data sets as in Fig. 4. Dashed vertical lines correspond to the threshold selected for each VOI.

3.1. Porosity

The data presented in Fig. 6 show that the segmented porosity decreases as the sample age increases. This trend held for all samples with the exception of two anomalies: the 100% slag and 100% fly ash samples each reported a slightly higher segmented porosity than the respective 3 day samples. These are the two samples identified earlier as presenting the greatest difficulty in greyscale threshold identification, which indicates that the manual threshold selection procedure which was required for these samples seems to slightly overestimate porosity.

Collins and Sanjayan [39] also found that the porosity of an alkali-activated 100% GGBFS binder with a w/b ratio of 0.5 decreased significantly over the first 90 days of reaction. This compares well with the trends observed in the current study, and is expected because hydration of slag-rich alkali-activated binders causes tortuosity to increase

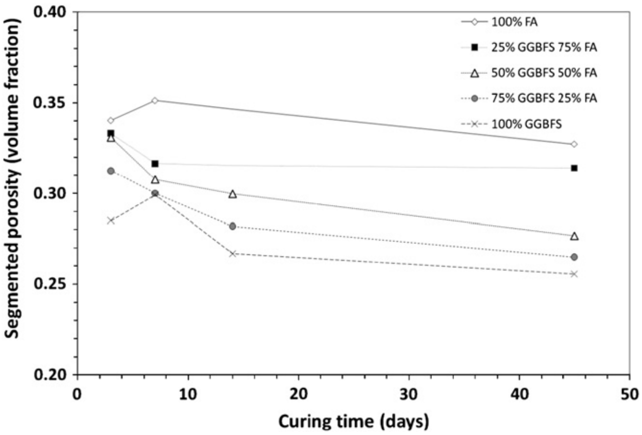

Fig. 6. Relationship between segmented porosity and curing time for all five sample compositions studied.

and porosity to decrease [39]. Sindhunata et al. [40] observed no significant change in the porosity of fly ash–NaOH and fly ash–Na silicate binders by nitrogen sorption porosimetry during the first 28 days of curing, but Park and Kang [41] observed a very marked decrease (from 32% at 1 day to 22.6% at 28 days) in fly ash–NaOH systems using mercury intrusion porosimetry. This may be related to the well-known difficulties associated with the accurate application of mercury intrusion to materials with complex, tortuous pore systems [13,42,43], where the tortuosity of the pore network plays a significant role in determining the measured porosity and pore size distribution. The nitrogen sorption study [40] also showed a refinement of the pore size, whereas the mercury intrusion study did not show any pore size refinement. The data presented in Fig. 6 agree more closely with the nitrogen sorption data of Sindhunata et al. [40] in that the overall difference in porosity between 3 and 45 days is only slight.

The substitution of fly ash for slag is seen in Fig. 6 to lead to higher porosity, with a monotonic increase observed when moving from 100% slag to 100% fly ash at every sample age studied. This is consistent with the results of nitrogen sorption analysis [13], and the numerical porosity data obtained by segmentation here are also similar to the values obtained in that study for samples with similar mix design, differing by less than 2 vol.% in absolute porosity for comparable mixes.

Such an increase in porosity with fly ash addition can also be predicted by consideration of the binder chemistry; the slag-rich systems predominantly form a C-(A)-S-H gel with a significant bound water content, while the fly ash-rich systems form N-A-S-(H), with a lower bound water content [1]. It has been suggested that the presence of more bound water, induced by the presence of extra Ca, will provide more pore-filling capacity — but previous data have not been fully convincing in supporting this point, particularly where the additional Ca was supplied from a Class C fly ash, and the dominant effect appeared to be pore refinement rather than an overall porosity reduction [13]. The results presented here show that, at least on the length scale of porosity which is able to be analysed at the voxel resolution available here, the coexistence of the Ca-rich and 'geopolymer' type gels seems to provide significant benefits over the aluminosilicate geopolymer gel alone, as the segmented porosities of the binders with GGBFS content of 50 wt.% or greater were significantly less at 45 days than those with a lower GGBFS content.

3.2. Tortuosity

Fig. 7 presents the calculated diffusion tortuosity of each sample as a function of age; the diffusion tortuosity increased with increasing sample age and as FA content decreased. The deviations from this trend were in the 100% slag and 100% fly ash samples after 7 days, which were problematic in the segmentation process as previously discussed (and even so, the 7-day 100% fly ash sample only shows a very slight decrease in tortuosity compared to the 3-day sample), and also the 50% slag/50% fly ash sample at 3 and 7 days. The reasons for the difference in behaviour of this last mix design are not clear; there are no immediately visible issues in the reconstructed data sets which could cause the tortuosity to deviate from the expected trends.

Fig. 8 shows the relationship between segmented porosity and tortuosity for the sample set analysed here. There is a direct relationship between these two parameters; tortuosity appears to vary inversely with porosity across these samples. The dashed line shows such an inverse relationship, with a horizontal asymptote at a tortuosity value of 1 (i.e., no resistance to diffusion at high porosity), and a vertical asymptote at a porosity value of 0.18, which is the percolation threshold obtained by Bentz and Garboczi [44] in their seminal modelling study of Portland cement (i.e., resistance to diffusion becomes infinite when the pore network is depercolated, assuming that the 'solid' phase in the segmented data sets is in fact solid — this will not actually be the case for a nanoporous gel binder, but provides a first approximation here). The assumption that the pore percolation threshold in alkali-activated binders is not too dissimilar from that of Portland cement remains to be tested, but appears useful here. The inverse relationship appears to describe the tortuosity of the pore network of the entire alkali-activated binder set very well, regardless of the marked difference in microstructure observed in Fig. 4 between the slag-rich and fly ash-rich binders, and may prove to be useful as a first approximation for estimating tortuosity values for use in diffusional transport simulations when only porosity data are available.

As tortuosity data for geopolymer binders have not previously been published, it is not possible to provide a direct comparison between the results presented here and any other results for similar samples. However, the diffusion tortuosity results are able to be compared with data obtained in a recent synchrotron radiation μCT study on OPC, carried out by Promentilla et al. [14]. In that study, two methods of segmentation are applied, which significantly impact the results obtained. The two methods are the transition point method, as previously discussed, and also the use of the Powers and Brownyard model for cement hydration to predict a theoretical porosity, which was then used to define the chosen threshold value. A summary of the results from both methods, and those obtained in the present study for the 100% GGBFS system, is shown in Table 2.

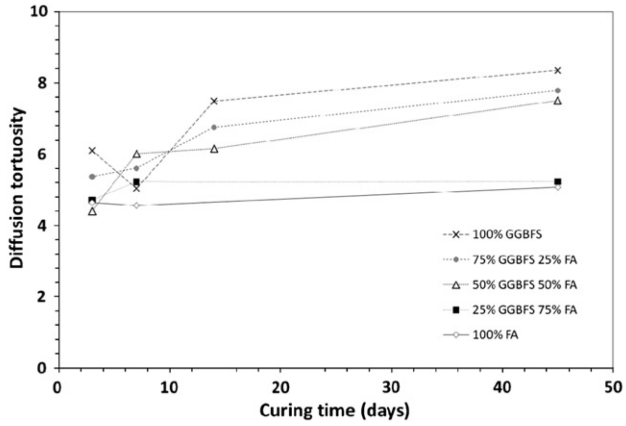

Fig. 7. Relationship between the diffusion tortuosity and curing time for all five sample compositions studied.

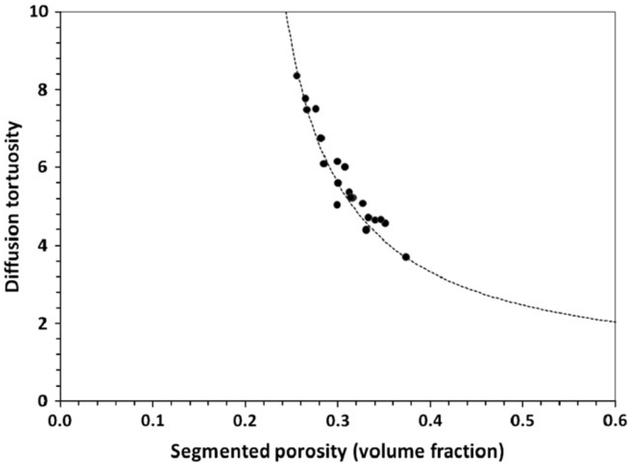

Fig. 8. Relationship between the segmented porosity and diffusion tortuosity for all samples studied. The dashed line is an inverse relationship, asymptoting to the percolation threshold of 0.18 and a tortuosity of 1, as detailed in the text.

The same trend is observed in the diffusion tortuosity over all three data sets — the tortuosity decreases as segmented porosity increases. However, the diffusion tortuosities obtained by Promentilla et al. [14] by the transition point method were much higher than those calculated here, whereas those obtained by using the theoretical hydration model were similar. This is because the segmented porosities of OPC binders obtained by the transition point method were close to the percolation limit, while the theoretical segmented porosities were well above the percolation limit [14], and are more comparable to those obtained in this study. Based on the similar orders of magnitude of chloride diffusion coefficients and gas and water permeabilities between OPC and alkali-activated binders, as shown throughout the literature, it seems more likely that a more accurate comparison is to be obtained by comparing the segmented porosities of alkali-activated binders obtained in this study with the 'theoretical' (Powers and Brownyard model-derived) data for OPC. Comparing these values with the data plotted in Fig. 8 shows that the 2-day and 7-day data points would be in good agreement with the trend observed for alkali-activated binders, but the 28-day tortuosity of OPC binders is significantly higher than the tortuosity of alkali-activated binders of similar porosity.

In the current sample set, the pore network in the VOI of every sample analysed contained a single percolating pore that accounted for over 95% of the segmented porosity, with the majority being on the order of 99%; much of the remaining pore space is inside hollow fly ash particles and thus inaccessible. Thus, the threshold values used here are well above the percolation limit. The identification of a single percolating pore network in the VOI is likely to be important in determining the binder characteristics, as transport through a percolated pore system is far more facile than when transport through the gel itself is required for diffusional transport to proceed [44].

3.3. Implications for durability of alkali-activated concretes

In general, as summarised in Table 3, alkali-activated binders with high GGBFS content show a greater extent of reduction in segmented porosity with extended curing duration, and a correspondingly greater increase in diffusion tortuosity, than do binders with high fly ash content. In particular, the pore volumes of high-FA binders did not vary much beyond 7 days of curing. This has a pronounced effect on the observed porosity and tortuosity values — GGBFS-rich binders show a considerably lower porosity and higher tortuosity than fly ash-rich systems, especially after longer curing durations.

As the porosity and tortuosity parameters obtained from the tomography data here provide an indication of the pore network geometry and microstructure, these data show that there will be more restriction on diffusion through GGBFS-rich binders than in FA-rich binders. This will be essential to the protection of embedded steel reinforcing from corrosion induced by loss of alkalinity (either due to alkali leaching by soft water, acid ingress, or carbonation), which is critical in the case of alkali-activated binders due to the absence of portlandite as a pH buffering phase within the binder when compared with hydrated OPC [12]. Binders rich in GGBFS are therefore expected on this basis to have a higher durability than FA-based binders; however, any differences in the strength of chemical binding of alkalis, carbonates and chlorides between C-(A)-S-H type gels and N-A-S-(H) gels may become significant in determining the actual relative performance, and such comparisons remain to be explored in detail in the literature.

Table 2
Comparison between the results (porosity φ and tortuosity τ_D) of the current study for silicate-activated GGBFS with w/b = 0.4, and literature data [14] for OPC pastes prepared with w/b = 0.5.

100% GGBFS (current study)			OPC, transition point [14]			OPC, theoretical [14]		
Age (days)	Φ	τ_D	Age (days)	φ	τ_D	Age (days)	φ	τ_D
3	0.28	6.1	2	0.18	18	2	0.40	3
14	0.27	7.5	7	0.15	26	7	0.34	5
45	0.26	8.4	28	0.14	118	28	0.31	9

The results of the tomographic analysis presented here indicate that the restriction of the pore structure is highly time dependent, particularly for binders with ≥50% GGBFS (and therefore a microstructure dominated by C-S-H type gels). From these data, it is possible to identify that the shift from N-A-S-(H) (low bound water) to C-(A)-S-H (high bound water content) occurs in this system between 25% and 50% GGBFS content. This is in good agreement with porosimetric data obtained for samples synthesised using the same fly ash at lower water/binder ratio and 28 days of curing [13]; in that data set, the 25% GGBFS sample showed a porosity similar to that of the 100% fly ash binder, and a marked decrease was obtained when moving to 50% and then 100% GGBFS. These data sets then provide a key piece of information regarding gel coexistence in blended alkali-activated systems; in this case, with less than 50% GGBFS added, it appears that there is not enough Ca present to induce the formation of specific Ca-rich gel phases, which suggests that there must be at least some extent of incorporation of Ca into the N-A-S-(H) gels formed at low calcium content. However, the strong distinction between the 25% and 50% GGBFS binders is not observed at early ages; it seems that the evolution of the space-filling nature of the C-(A)-S-H gel structure requires a reasonably extended period of curing in these systems. This is consistent with the well-known sensitivity of alkali-activated binders to curing conditions, and in particular to the availability of a sufficient supply of water (via sealed, wet or steam curing) in the first few weeks.

4. Conclusions

Alkali-activated binder composition and curing time have both been shown to have a significant impact on the microstructural and pore network properties of the hardened material, as determined by synchrotron X-ray microtomography for a set of sodium metasilicate-activated ground granulated blast furnace slag/fly ash pastes. Longer curing times and higher slag content gave an increase in pore network tortuosity and a decrease in total porosity, and this was particularly notable at slag contents of 50% or higher. This indicates that the formation of space-filling C-(A)-S-H gels begins to dominate the alkali-activated binder system between 25% and 50% slag content, where samples with 25% or lower slag contents are instead dominated by N-A-S-(H) gels, which do not chemically bind water and therefore do not provide the same extent of pore network obstruction.

This study has provided the first ever systematic three-dimensional analysis of alkali-activated binder structures by high-resolution X-ray microtomography, and provides the first steps towards a complete understanding of the pore network geometry in a way that is not achievable using two-dimensional techniques such as electron microscopy. There remain difficulties in the accurate identification of pore and solid regions in alkali-activated binder systems due to the low elemental number, and therefore low X-ray absorption contrast, in these materials. Phase contrast tomography does provide the potential for advances in this area, but is also non-trivial to implement. The voxel resolution of even highly advanced synchrotron microtomography instruments is also significantly coarser than the intrinsic (nanoscale) porosity of the binder phases, necessitating further developments in the application of nanotomography before a fully representative picture of the pore networks can be generated. Nonetheless, the suite of data presented here provide valuable information regarding porosity, pore geometry and tortuosity within a large systematic set of samples, and provide a strong basis for future developments in this area as both the available instrumentation and the understanding of alkali-activated binder structure are developed further in the future.

Acknowledgements

This work was funded by the Australian Research Council (ARC), including some funding through the Particulate Fluids Processing Centre, a Special Research Centre of the ARC, and also via a Linkage Project grant co-sponsored by the ARC and Zeobond Research. Travel funding for J.L. Provis to conduct experimental work at Argonne National Laboratory was provided by the Banksia Environmental Foundation through the award of the Brian Robinson Fellowship. We also thank Adam Kilcullen for his assistance in conducting the sample synthesis, and Dr Xianghui Xiao and Dr Francesco de Carlo for assistance in the data collection and processing on the 2BM instrument. Use of the Advanced Photon Source was supported by the U.S. Department of Energy, Office of Science, Office of Basic Energy Sciences, under Contract DE-AC02-06CH11357. Special thanks are also due to Dr Y. Nakashima and Dr S. Kayima, the authors of reference [34], as their freely available Mathematica 5.2 scripts *Clabel.nb*, *Pre_Rwalk_image.nb* and *Rwalk.nb* were instrumental in enabling the tortuosity calculations presented in this study, and to an anonymous reviewer for insightful comments which have helped to improve the manuscript.

References

[1] M.C.G. Juenger, F. Winnefeld, J.L. Provis, J. Ideker, Advances in alternative cementitious binders, Cem. Concr. Res. 41 (2011) 1232–1243.

[2] J.L. Provis, J.S.J. van Deventer, Geopolymers: Structures, Processing, Properties and Industrial Applications, Woodhead, Cambridge, UK, 2009 448pp.

[3] C. Shi, P.V. Krivenko, D.M. Roy, Alkali-Activated Cements and Concretes, Taylor & Francis, Abingdon, UK, 2006 376pp.

[4] P. Duxson, J.L. Provis, G.C. Lukey, J.S.J. van Deventer, The role of inorganic polymer technology in the development of 'green concrete', Cem. Concr. Res. 37 (2007) 1590–1597.

[5] J.L. Provis, P. Duxson, J.S.J. van Deventer, The role of particle technology in developing sustainable construction materials, Adv. Powder Technol. 21 (2010) 2–7.

[6] P. Duxson, J.L. Provis, Designing precursors for geopolymer cements, J. Am. Ceram. Soc. 91 (2008) 3864–3869.

[7] F. Puertas, A. Fernández-Jiménez, Mineralogical and microstructural characterisation of alkali-activated fly ash/slag pastes, Cem. Concr. Compos. 25 (2003) 287–292.

[8] J.S.J. van Deventer, J.L. Provis, P. Duxson, D.G. Brice, Chemical research and climate change as drivers in the commercial adoption of alkali activated materials, Waste Biomass Valorization 1 (2010) 145–155.

[9] K.C. Goretta, N. Chen, F. Gutierrez-Mora, J.L. Routbort, G.C. Lukey, J.S.J. van Deventer, Solid-particle erosion of a geopolymer containing fly ash and blast-furnace slag, Wear 256 (2004) 714–719.

[10] Z. Li, S. Liu, Influence of slag as additive on compressive strength of fly ash-based geopolymer, J. Mater. Civil Eng. 19 (2007) 470–474.

[11] F. Puertas, S. Martínez-Ramírez, S. Alonso, E. Vázquez, Alkali-activated fly ash/slag cement. Strength behaviour and hydration products, Cem. Concr. Res. 30 (2000) 1625–1632.

[12] R.R. Lloyd, J.L. Provis, J.S.J. van Deventer, Pore solution composition and alkali diffusion in inorganic polymer cement, Cem. Concr. Res. 40 (2010) 1386–1392.

[13] R.R. Lloyd, J.L. Provis, K.J. Smeaton, J.S.J. van Deventer, Spatial distribution of pores in fly ash-based inorganic polymer gels visualised by Wood's metal intrusion, Microporous Mesoporous Mater. 126 (2009) 32–39.

[14] M.A.B. Promentilla, T. Sugiyama, T. Hitomi, N. Takeda, Quantification of tortuosity in hardened cement pastes using synchrotron-based X-ray computed microtomography, Cem. Concr. Res. 39 (2009) 548–557.

[15] J.L. Provis, J.S.J. van Deventer, Geopolymerisation kinetics. 2. Reaction kinetic modelling, Chem. Eng. Sci. 62 (2007) 2318–2329.

[16] W.M. Kriven, J.L. Bell, M. Gordon, Microstructure and nanoporosity in as-set geopolymers, Ceram. Eng. Sci. Proc. 27 (2006) 313–324.

[17] F. Collins, J.G. Sanjayan, Effect of pore size distribution on drying shrinking of alkali-activated slag concrete, Cem. Concr. Res. 30 (2000) 1401–1406.

[18] D.P. Bentz, S. Mizell, S. Satterfield, J. Devaney, W. George, P. Ketcham, J. Graham, J. Porterfield, D. Quenard, F. Vallee, H. Sallee, E. Boller, J. Baruchel, The visible cement data set, J. Res. Natl. Inst. Stand. Technol. 107 (2002) 137–148.

[19] P.J.M. Monteiro, A.P. Kirchheim, S. Chae, P. Fischer, A.A. MacDowell, E. Schaible, H.R. Wenk, Characterizing the nano and micro structure of concrete to improve its durability, Cem. Concr. Compos. 31 (2009) 577–584.

[20] U. Rattanasak, K. Kendall, Pore structure of cement/pozzolan composites by X-ray microtomography, Cem. Concr. Res. 35 (2005) 637–640.

[21] L. Helfen, E. Dehn, P. Mikulik, T. Baumbach, Three-dimensional imaging of cement microstructure evolution during hydration, Adv. Cem. Res. 17 (2005) 103–111.

[22] E.N. Landis, A.L. Petrell, S. Lu, E.N. Nagy, Examination of pore structure using three-dimensional image analysis of microtomographic data, Concr. Sci. Eng. 2 (2000) 162–169.

[23] S. Diamond, E.N. Landis, Microstructural features of a mortar as seen by computed microtomography, Mater. Struct. 40 (2007) 989–993.

[24] T. Sugiyama, M.A.B. Promentilla, T. Hitomi, N. Takeda, Application of synchrotron microtomography for pore structure characterization of deteriorated cementitious materials due to leaching, Cem. Concr. Res. 40 (2010) 1265–1270.

[25] S.R. Stock, Recent advances in X-ray microtomography applied to materials, Int. Mater. Rev. 53 (2008) 129–181.

[26] J.L. Provis, V. Rose, R.P. Winarski, J.S.J. van Deventer, Hard X-ray nanotomography of amorphous aluminosilicate cements, Scr. Mater. 65 (2011) 316–319.

[27] P. Trtik, B. Münch, P. Gasser, A. Leemann, R. Loser, R. Wepf, P. Lura, Focussed ion beam nanotomography reveals the 3D morphology of different solid phases in hardened cement pastes, J. Microsc. 241 (2011) 234–242.

[28] Y.X. Wang, F. De Carlo, D.C. Mancini, I. McNulty, B. Tieman, J. Bresnahan, I. Foster, J. Insley, P. Lane, G. von Laszewski, C. Kesselman, M.H. Su, M. Thiebaux, A high-throughput x-ray microtomography system at the Advanced Photon Source, Rev. Sci. Instrum. 72 (2001) 2062–2068.

[29] E.J. Garboczi, D.P. Bentz, The effect of statistical fluctuation, finite size error, and digital resolution on the phase percolation and transport properties of the NIST cement hydration model, Cem. Concr. Res. 31 (2001) 1501–1514.

[30] H. Uchikawa, Similarities and discrepancies of hardened cement paste, mortar and concrete from the standpoints of composition and structure, J. Res. Onoda Cem. Company 40 (1988) 88–121.

[31] E. Gallucci, K. Scrivener, A. Groso, M. Stampanoni, G. Margaritondo, 3D experimental investigation of the microstructure of cement pastes using synchrotron X-ray microtomography (μCT), Cem. Concr. Res. 37 (2007) 360–368.

[32] M.A.B. Promentilla, T. Sugiyama, T. Hitomi, N. Takeda, Characterizing the 3D pore structure of hardened cement paste with synchrotron microtomography, J. Adv. Concr. Technol. 6 (2008) 273–286.

[33] R.R. Lloyd, J.L. Provis, J.S.J. Van Deventer, Microscopy and microanalysis of inorganic polymer cements. 1: remnant fly ash particles, J. Mater. Sci. 44 (2009) 608–619.

[34] Y. Nakashima, S. Kamiya, Mathematica programs for the analysis of three-dimensional pore connectivity and anisotropic tortuosity of porous rocks using X-ray computed tomography image data, J. Nucl. Sci. Technol. 44 (2007) 1233–1247.

[35] J. Hoshen, R. Kopelman, Percolation and cluster distribution. I. Cluster multiple labeling technique and critical concentration algorithm, Phys. Rev. B 14 (1976) 3438.

[36] R.J. Myers, Analysing geopolymer pore structures through X-ray microtomography, Research Report, Department of Chemical & Biomolecular Engineering, University of Melbourne, 2010 36pp.

[37] R.R. Lloyd, J.L. Provis, J.S.J. Van Deventer, Microscopy and microanalysis of inorganic polymer cements. 2: the gel binder, J. Mater. Sci. 44 (2009) 620–631.

[38] H. Zhou, X. Wu, Z. Xu, M. Tang, Kinetic study on hydration of alkali-activated slag, Cem. Concr. Res. 23 (1993) 1253–1258.

[39] F.G. Collins, J.G. Sanjayan, Capillary shape: influence on water transport within unsaturated alkali activated slag concrete, J Mater Civil Eng 22 (2010) 260–266.

[40] Sindhunata, J.L. Provis, G.C. Lukey, H. Xu, J.S.J. van Deventer, Structural evolution of fly ash-based geopolymers in alkaline environments, Ind. Eng. Chem. Res. 47 (2008) 2991–2999.

[41] S.-S. Park, H.-Y. Kang, Strength and microscopic characteristics of alkali-activated fly ash-cement, Korean J. Chem. Eng. 23 (2006) 367–373.

[42] S. Diamond, Mercury porosimetry. An inappropriate method for the measurement of pore size distributions in cement-based materials, Cem. Concr. Res. 30 (2000) 1517–1525.

[43] Sindhunata, J.S.J. van Deventer, G.C. Lukey, H. Xu, Effect of curing temperature and silicate concentration on fly-ash-based geopolymerization, Ind Eng Chem Res 45 (2006) 3559–3568.

[44] D.P. Bentz, E.J. Garboczi, Percolation of phases in a three-dimensional cement paste microstructural model, Cem. Concr. Res. 21 (1991) 325–344.